Anthraquinone-Enriched Conjugated Microporous Polymers as Organic Cathode Materials for High-Performance Lithium-Ion Batteries

Mohamed Gamal Mohamed,*,[⊥] Santosh U. Sharma,[⊥] Cheng-Han Yang, Maha Mohamed Samy, Ahmed A. K. Mohammed, Swetha V. Chaganti, Jyh-Tsung Lee,* and Shiao Wei-Kuo*

Cite This: *ACS Appl. Energy Mater.* 2021, 4, 14628−14639

Read Online

ACCESS | Metrics & More | Article Recommendations | Supporting Information

ABSTRACT: Extended π-conjugated microporous polymers (CMPs) are useful as organic anode or cathode materials in lithium-ion batteries (LIBs), overcoming the issue of small organic molecules becoming soluble in the electrolytes during charge–discharge cycles. In this study, we constructed two CMPs (Py-A-CMP, TPE-A-CMP) containing anthraquinone (A) moieties (as redox-active units and sources of C=O groups) and applied them as organic cathodes in LIBs. We synthesized the Py-A-CMP and TPE-A-CMP through Sonogashira–Hagihara couplings of 2,6-dibromoanthraquinone (A-Br$_2$) with tetraethynylpyrene (Py-T) and tetraethynyltetraphenylethene (TPE-T), respectively. The TPE-A-CMP displayed high thermal decomposition temperatures (up to 539 °C) and char yields (up to 53 wt %). Electrochemical tests revealed that Py-A-CMP and TPE-A-CMP delivered discharge capacities (196.6 and 164.7 mAh g^{-1} at a C-rate of 0.1C, respectively) higher than those of other CMP materials. The capacity retention of TPE-A-CMP was 163 mAh g^{-1} (99.3%) over 400 cycles. The corresponding cells incorporating Py-T-CMP and TPE-T-CMP also exhibited excellent rate capability performance, maintaining discharge capacities of approximately 79 and 49 mAh g^{-1}, respectively, at a high charge/discharge rate of 5C. Scanning electron microscopy confirmed the superior stability of both CMPs, revealing that these electrode materials remained intact, without any surface crack formation, during long-term cycling.

KEYWORDS: conjugated microporous polymers, anthraquinone, Sonogashira–Hagihara couplings, thermal stability, lithium-ion batteries
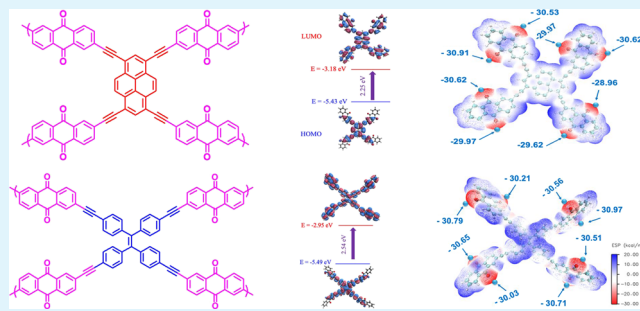
INTRODUCTION

Our technical and industrial world demands greater energy generation, conversion, and storage. Energy storage systems (ESSs) allow us to stockpile energy created using conventional and sustainable power sources (e.g., solar, water, wind, and waste energy) for electric vehicles.[1] Solar cells, fuel cells, and rechargeable batteries have become fundamental tools for energy storage, with lithium-ion batteries (LIBs) having gained great popularity because of their low ecological footprint, high energy density, and good cycle life. Nevertheless, LIBs have major drawbacks, including their carbon anodes having a theoretical capacity of only 372 mAh g^{-1}, which must be addressed.[2−4] At present, lithium batteries often contain poisonous metals, which bring into consideration huge energy utilization and climate contamination, particularly for bulk energy storage applications.[5−7] Although industrially used LIBs have electrodes of inorganic origin, these materials are hazardous and scarce, leading to sustainability issues.[8] The advancement of organic cathode materials for battery-powered applications has been moderate in comparison with that of inorganic cathode materials.[9−11] Organic materials have unique advantages when used as cathode materials, including facile molecular engineering,[2,12] low cost, high abundance, environmental friendliness, and high theoretical capacities.[11] One of the greatest attractions of organic molecules is their chemical diversity.[13] The most widely investigated organic materials for LIBs include conjugated polymers,[14,15] organic radical polymers,[11] organosulfur compounds,[11,15−17] and C=O- and C/N-based compounds.[16,17] Unfortunately, rapid capacity decay and low cycling stability are often observed with these organic materials due to their high solubility in electrolytes, thereby limiting their applicability[2,18] Many attempts have been made to overcome this solubility issue, including the addition of conductive carbons to ensure firmer structures[2,19] and the polymerization of various molecules.[20,21] Rapid
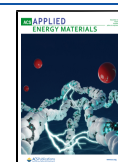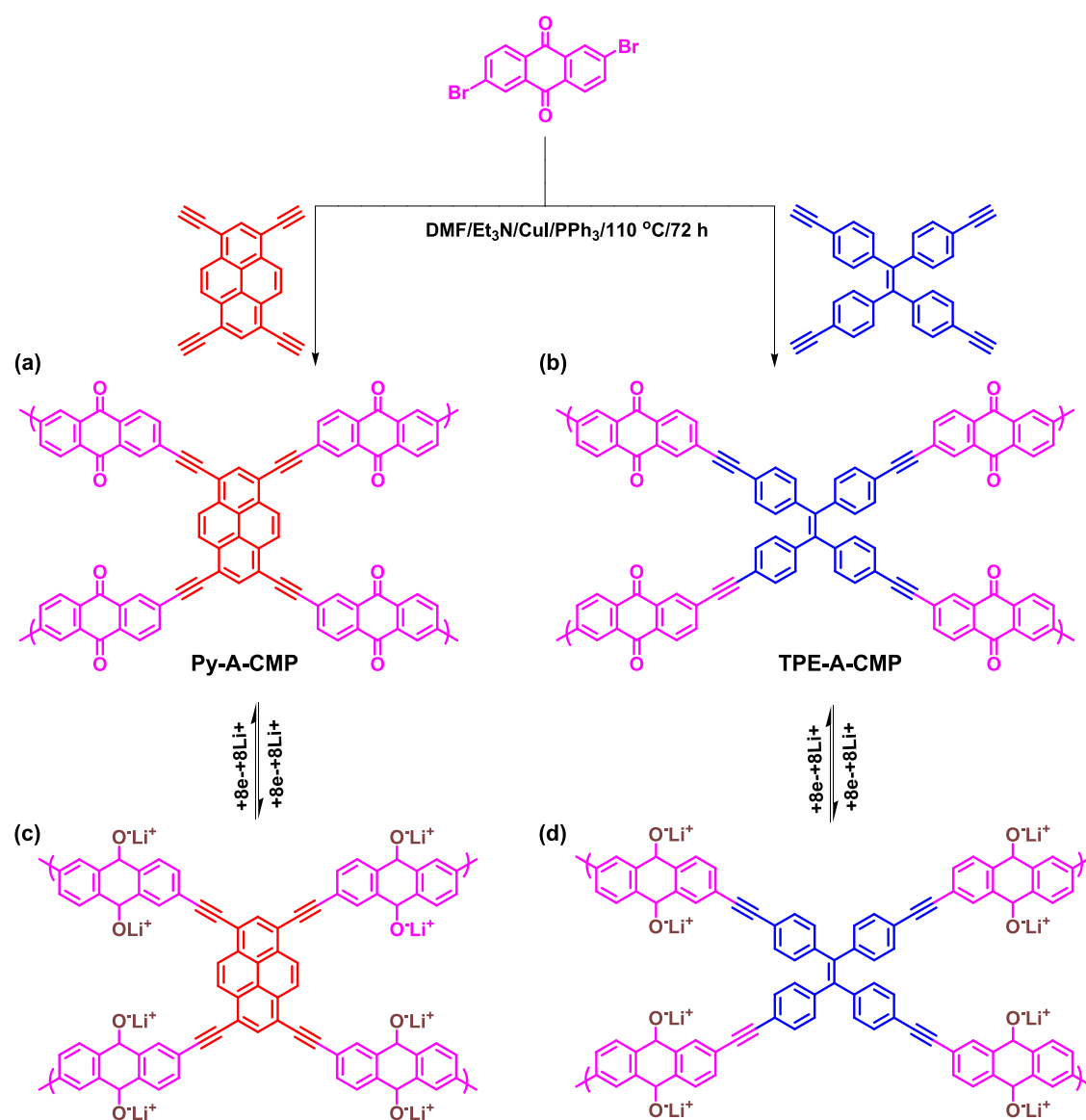
Figure 1. Schematic representation of the preparation of (a) Py-A-CMP and (b) TPE-A-CMP. Electrochemical lithiation and delithiation of (c) Py-A-CMP/Li and (d) TPE-A-CMP/Li cells.

capacity decay and low cycling stability can also arise because of narrow band gaps and greater conjugation when incorporating redox-active sites and organic conjugated frameworks in porous organic molecules.[11,22,23]

Creative and challenging approaches will be needed to address the notable drawbacks of present-day ESSs and improve the capacities of their electrode materials. Research into the development of superconductors has shifted recently toward porous organic materials.[11,24−28] These materials, which are generally connected by covalent bonds, have attracted much attention as advanced functional materials. Porous organic polymers (POPs), including hypercrosslinked polymers (HCPs), covalent organic frameworks (COFs), and conjugated microporous polymers (CMPs), have been prepared with various properties for a broad range of potential applications.[29−39] In addition, redox-active organic molecules can be suitable for use as electrode materials because of their excellent electrochemical performance, simple structural design, and excellent chemical and physical properties.[1] CMPs are particularly useful for their good stability, excellent

processability, and ease of fabrication.[1,40] Indeed, organic CMPs can be synthesized readily on large scales from renewable raw materials, at low temperatures and with low amounts of generated waste.[1] The amalgamation of organic CMPs with other substances (e.g., organic frameworks, nanoarchitectures, colloids, and porous materials) can produce smart materials—another advantage to their use in ESSs.[1,21,41−43] A variety of redox-active organic molecules have been explored as active materials, containing, for example, C=O, nitroxyl, phenoxy, and viologen units; among them, quinones (especially anthraquinones) have been widely applied as active materials because of their structural diversity, tunable redox potentials, high theoretical capacities (owing to their ability to add $2e^-/2Li^+$ per quinone unit), high rates of redox reactions, and environmental friendliness.[44−53] With their many appealing properties, CMPs have found applications in catalysis,[54] gas storage and separation,[55] sensing,[56] and light harvesting.[57]

Conjugated porous polymers (CPPs) have also received much attention because of their high physical and chemical

stabilities, high specific surface areas, and tunable porous structures; they are typically categorized as either crystalline porous materials or amorphous polymers. Among them, CMPs and COFs have become popular for electrochemical energy storage applications for the following reasons: (i) the ease of construction of various molecules and active sites for electrode application; (ii) their ability to facilitate charge transport (i.e., through electrolyte infiltration, due to high porosity, thereby controlling stress/strain during electrochemical reactions); (iii) charge delocalization facilitated as a result of π-conjugated structures; and (iv) the ability to form two-dimensional (2D) and three-dimensional (3D) structures with high surface areas, thereby improving electrochemical kinetics. The uncomplicated structures and feasible tunability of CMPs (with a diversity of redox-active moieties) can result in LIBs displaying high reversibility and cyclability, with all of the properties of CMPs suitable for exploitation to collaboratively improve the performance.[58] For example, Si et al. prepared a PT-BTA CMP (featuring pyrene-4,5,9,10-tetraone moieties as redox-active groups) as a cathode material for LIBs, observing a capacitance of 166.7 mAh g^{-1} and good cycling stability.[59] A HATN-CMP (based on hexaazatrinaphthalene units) has been used as a cathode material in LIBs, providing a capacitance of 147 mAh g^{-1}.[60] Liu and co-workers reported an AQ@N-ZIF-8 cathode having a high specific capacity (240 mAh g^{-1} at 0.1C).[61] In addition, Yang and co-workers found that a 3D-Azo-CTF cathode material for LIBs exhibited good capacity retention, cycle life, and capacitance (205.6 mAh g^{-1}).[62] Zhuang et al. prepared BQbTPL through Diels−Alder reactions; it displayed an excellent performance rate, high capacitance charge (152.9 mAh g^{-1}), and a stable structure.[63]

To the best of our knowledge, this paper is the first to report CMP materials containing pyrene and tetraphenylethylethene (TPE) units (as core building blocks) and anthraquinone units (as redox-active groups) for application as organic cathodes in LIBs. We have prepared two CMPs, named Py-A-CMP and TPE-A-CMP, through Sonogashira−Hagihara cross-couplings of 2,6-dibromoanthraquinone (A-Br$_2$) with tetraethynylpyrene (Py-T) and 1,1,2,2-tetrakis(4-ethynylphenyl)ethene (TPE-T) in the presence of a Pd catalyst (Figure 1a,b). We characterized these materials in terms of their chemical structures, Brunauer−Emmett−Teller (BET) surface areas, pore size diameters, morphologies, thermal stabilities, and crystallinities. We then investigated the electrochemical performance of our as-prepared CMP-based polymers as cathode materials; Py-A-CMP and TPE-A-CMP displayed high initial capacities (180 and 161 mAh g^{-1}, respectively), with superior rate capabilities and capacitively controlled lithium-ion kinetics as calculated. These compounds also demonstrated high Coulombic efficiencies (99.9%) throughout the duration of testing.

■ EXPERIMENTAL SECTION

Materials. Palladium tetrakis(triphenylphosphine) [Pd(PPh$_3$)$_4$] and lithium bis(trifluoromethanesulfonyl)imide (LiTFSi, 99%) were obtained from Sigma-Aldrich. Potassium carbonate (99.9%), benzophenone (99%), anhydrous triethylamine (Et$_3$N, 99%), methanol (MeOH), bromine (Br$_2$), chloroform (CHCl$_3$), titanium tetrachloride (TiCl$_4$, 99.9%), acetone (CH$_3$COCH$_3$), triphenylphosphine (PPh$_3$, 99%), pyrene (98%), zinc (Zn, 98%), tetrahydrofuran (THF), 2,6-diaminoanthraquinone (A-2NH$_2$), copper(I) iodide (CuI, 99%), anhydrous magnesium sulfate (MgSO$_4$, 99.5%), (trimethylsilyl)acetylene (98%), 1,3-dioxolane (DOL, 99.5%), and dimethoxyethane (DME) were purchased from Alfa Aesar. Poly(vinylidene difluoride) (PVDF) was purchased from Acros. Other solvents were used as

received commercially, without any purification. Tetraphenylethylene (TPE), 1,1,2,2-tetrakis(4-bromophenyl)ethene (TPE-Br$_4$), and 1,3,6,8-tetrabromopyrene (Py-Br$_4$) were prepared according to a previous report (Figures S1−S7).[24,30,32,36]

1,3,6,8-Tetrakis(2-(trimethylsilyl)ethynyl)pyrene (Py-TMS). Pd(PPh$_3$)$_4$ (0.330 g, 0.450 mmol), PPh$_3$ (0.366 g, 1.38 mmol), Py-Br$_4$ (3.00 g, 5.79 mmol), CuI (0.120 g, 0.930 mmol), and Et$_3$N/toluene (1:1, v/v; 80 mL) were charged into a two-neck round-bottom flask (100 mL), and then the mixture was heated under N$_2$ for 30 min at 50 °C. After 30 min, ethynyltrimethylsilane (4.56 g, 46.4 mmol) was added dropwise over 10 min, and then the mixture was heated under reflux for 48 h at 80 °C. The remaining residue was extracted with water and CH$_2$Cl$_2$ to afford Py-TMS as an orange solid (2.80 g, 93%: Scheme S1). The temperature for onset of decomposition: 350 °C. Fourier transform infrared spectroscopy (FTIR) (KBr, cm^{-1}, Figure S8): 3053 (aromatic C−H stretching), 2908 (aliphatic C−H stretching), 2100 (C≡C stretching). ^{1}H NMR (500 MHz, CDCl$_3$, δ, Figure S9): 8.60 (s, 4H), 8.30 (s, 2H), 0.413 (s, CH$_3$). ^{13}C NMR (125 MHz, CDCl$_3$, δ, Figure S10): 135.70, 132.40, 127.80, 119.20, 103.50, 101.60. (+)ESI-MS m/z 587.3 (calcd for C$_{36}$H$_{42}$Si$_4$) (Figure S11).

1,3,6,8-Tetraethynylpyrene (Py-T). A mixture of Py-TMS (1.59 g, 2.60 mmol) and K$_2$CO$_3$ (2.81 g, 20.4 mmol) in MeOH (40 mL) was stirred in a one-neck round-bottom flask (50 mL) for 24 h at room temperature. The reaction mixture was poured into 50 mL of water to remove K$_2$CO$_3$. The resulting brown precipitate was filtrated and dried at 60 °C to afford a brown solid (1.20 g, 75%: Scheme S1). Temperature for onset of decomposition: 350 °C. FTIR (KBr, cm^{-1}, Figure S12): 3279 (≡C−H), 2186 (C≡C stretching). ^{1}H NMR (500 MHz, CDCl$_3$, δ, Figure S13): 8.70 (s, 4H), 8.40 (s, 2H), 3.70 (s, 4H). ^{13}C NMR (125 MHz, CDCl$_3$, δ, Figure S14): 133.80, 130.80, 129.10, 127.80, 84.50, 59.70. (+)ESI-MS m/z 298.8 (calcd for C$_{24}$H$_{10}$) (Figure S15).

1,1,2,2-Tetrakis(4-((trimethylsilyl)ethynyl)phenyl)ethane (TPE-TMS). Pd(PPh$_3$)$_4$ (0.260 g, 0.360 mmol), PPh$_3$ (0.300 g, 1.14 mmol), TPE-Br$_4$ (3.00 g, 4.62 mmol), CuI (0.141 g, 0.430 mmol), and Et$_3$N/toluene (1:1, v/v; 40 mL) were charged into a two-neck round-bottom flask (100 mL), and then the mixture was heated under reflux for 30 min at 50 °C under N$_2$. Ethynyltrimethylsilane (3.64 g, 37.0 mmol) was added dropwise over 10 min and then the mixture was heated under reflux for 48 h at 80 °C. The remaining residue was extracted with water and CH$_2$Cl$_2$ to afford TPE-TMS as a pale-yellow powder (2.00 g, 66%: Scheme S2). The temperature for onset of decomposition: 200 °C. FTIR (KBr, cm^{-1}, Figure S16): 3060 (aromatic C−H stretching), 2155 (C≡C stretching). ^{1}H NMR (500 MHz, CDCl$_3$, δ, Figure S17): 7.24 (d, 8H), 6.90 (d, 8H), 0.22 (s, CH$_3$). ^{13}C NMR (125 MHz, CDCl$_3$, δ, Figure S18): 144, 141, 132.7, 132, 122.3, 105.6, 95.8. (+)ESI-MS m/z 717.4 (calcd for C$_{46}$H$_{52}$Si$_4$) (Figure S19).

Tetrakis(4-ethynylphenyl)ethylene (TPE-T). A mixture of TPE-TMS (1.0 g, 1.33 mmol) and K$_2$CO$_3$ (1.80 g, 13.31 mmol) in anhydrous MeOH (15 mL) was stirred in a one-neck round-bottom flask (50 mL) for 24 h at room temperature. The reaction mixture was poured into 50 mL of water to remove K$_2$CO$_3$. The resulting precipitate was filtrated and dried at 60 °C to afford TPE-T as a pale-yellow powder (1.40 g, 77%, Scheme S2). T_m: 155.5 °C. FTIR (KBr, cm^{-1}, Figure S20): 3273 (≡C−H), 2109 (C≡C stretching). ^{1}H NMR (500 MHz, CDCl$_3$, δ, Figure S21): 7.24 (d, 8H), 6.93 (d, 8H), 3.06 (s, 4H, ≡C−H). ^{13}C NMR (125 MHz, CDCl$_3$, δ, Figure S22): 83.6 (≡C−Ar), 77.88 (≡C−H). (+)ESI-MS m/z 428 (calcd for C$_{34}$H$_{20}$) (Figure S23).

2,6-Dibromoanthraquinone (A-Br$_2$). tert-Butyl nitrite (12 mL) was added to a solution of A-2NH$_2$ (3.00 g, 12.6 mmol) and CuBr$_2$ (7.04 g, 31.5 mmol) in dry MeCN (100 mL) in a 250 mL flask. After heating the mixture under reflux for 24 h at 70 °C, 6 M HCl (200 mL) was added dropwise. The brown solid was filtered off and washed with MeCN, MeOH, and water to afford A-Br$_2$ (2.20 g, 73%). Mp: 285−287 °C. ^{1}H NMR (500 MHz, CDCl$_3$, δ, Figure S24): 8.44 (d, 2H), 8.20 (d, 2H), 7.94 (d, 2H). ^{13}C NMR (125 MHz, CDCl$_3$, δ,
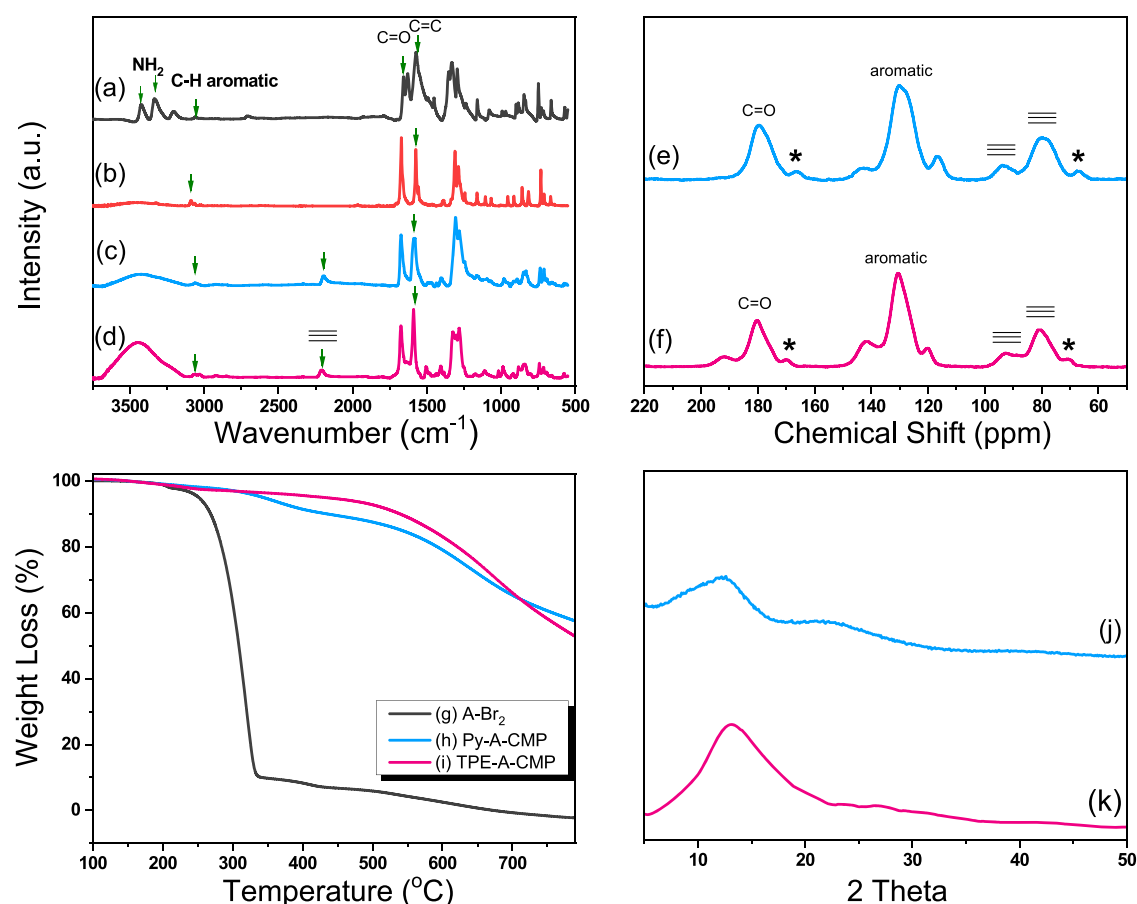
Figure 2. FTIR spectra of (a) A-2NH$_2$, (b) A-Br$_2$, (c) Py-A-CMP, and (d) TPE-A-CMP. Solid-state ^{13}C NMR spectra of (e) Py-A-CMP and (f) TPE-A-CMP. TGA profiles of (g) A-Br$_2$, (h) Py-A-CMP, and (i) TPE-A-CMP. (j, k) PXRD analyses of (j) Py-A-CMP and (k) TPE-A-CMP.

Figure S25): 179.66, 135.89, 132.97, 130.41, 128.83, 128.68, 127.60. (+)ESI-MS *m/z* 366 (calcd for C$_{14}$H$_6$Br$_2$O$_2$) (Figure S26).

Py-A-CMP. A solution of Py-T (150 mg, 0.470 mmol), A-Br$_2$ (137 mg, 0.750 mmol), CuI (9 mg, 0.05 mmol), PPh$_3$ (13 mg, 0.050 mmol), and Pd(PPh$_3$)$_4$ (57 mg, 0.050 mmol) in dimethylformamide (DMF) and Et$_3$N (10 mL) was heated at 110 °C for 72 h. The resulting insoluble solid was filtered off and washed with THF, MeOH, and acetone. The solid was dried under vacuum at 90 °C for 24 h to afford a dark-brown solid (80%). FTIR (KBr, cm^{-1}): 3057 (aromatic C−H), 2201 (C≡C), 1674.44 (C=O), 1586 (C=C).

TPE-A-CMP. TPE-A-CMP was prepared as a yellow-brown solid (85%) using the method described above, from TPE-T (150 mg, 0.470 mmol), A-Br$_2$ (126 mg, 0.750 mmol), CuI (9 mg, 0.05 mmol), PPh$_3$ (13 mg, 0.050 mmol), and Pd(PPh$_3$)$_4$ (57 mg, 0.050 mmol). FTIR (KBr, cm^{-1}): 3056.65 (aromatic C−H), 2212.13 (C≡C), 1669.33 (C=O), 1585.56 (C=C).

Py-A-CMP and TPE-A-CMP Electrodes for Electrochemical Measurements. Slurries for the working electrodes were prepared by mixing 40% of the active material (Py-A-CMP or TPE-A-CMP), 50% of the carbon-based conductive material (super P), and 10% of the binder (PVDF) in *N*-methyl pyrrolidone (NMP, 1 mL) and then stirring thoroughly for 24 h at room temperature. Each slurry was uniformly cast onto an Al foil using a doctor's blade and then dried at 100 °C for 12 h. The electrodes were punched in circular pieces using an electrode puncture device and transferred to an Ar-filled glovebox, where coin cells were fabricated against a Li foil (as the counter electrode) using a Celgard 2500 PP membrane and 1.0 M LiTFSi in DOL/DME (1:1, v/v) as the electrolyte. Cyclic voltammetry (CV) and alternating current (AC) impedance spectroscopy were performed using a CHI 750 (CH instruments); battery character-ization was performed using a LANHE CT 2001A.

■ RESULTS AND DISCUSSION

Preparation of Anthraquinone-Enriched CMPs (Py-A-CMP and TPE-A-CMP). We used Sonogashira−Hagihara coupling to prepare Py-A-CMP and TPE-A-CMP, featuring pyrene and tetraphenylethene units, respectively, as electron-donating moieties and anthraquinone as the electron-with-drawing moieties, as presented in Figure 1a,b. The Sonogashira−Hagihara couplings of 2,6-dibromoanthraqui-none (A-Br$_2$) with 1,3,6,8-tetraethynylpyrene (Py-T) and tetraethynyltetraphenylethene (TPE-T), respectively, in the presence of catalytic Pd(PPh$_3$)$_4$ at 110 °C for 3 days, afforded a red powder for Py-A-CMP and a yellow solid for TPE-A-CMP. The resulting CMPs were carefully washed with DMF, THF, acetone, and MeOH to remove any excesses of the unreacted monomers and Pd catalyst. Figure 2 presents the FTIR spectra of A-2NH$_2$, A-Br$_2$, Py-A-CMP, and TPE-A-CMP measured at room temperature. The FTIR spectrum of A-2NH$_2$ (Figure 2a) featured five major absorption bands at 3419 and 3336 cm^{-1} for the stretching of the amino groups, 3056 cm^{-1} for stretching of the C−H aromatic units, 1663 cm^{-1} for the C=O groups, and 1620 cm^{-1} for the C=C units. The FTIR spectrum of A-Br$_2$ (Figure 2b) featured absorption bands centered at 3089 and 1669 cm^{-1}, representing stretching of the aromatic C−H and C=O bonds in the anthraquinone moiety; the absence of any absorption bands of the amino groups confirmed the complete conversion of A-2NH$_2$ to A-Br$_2$. The FTIR spectra of Py-A-CMP and TPE-A-CMP (Figure 2c,d) featured absorption peaks at 3056, 2212−2200, 1669−
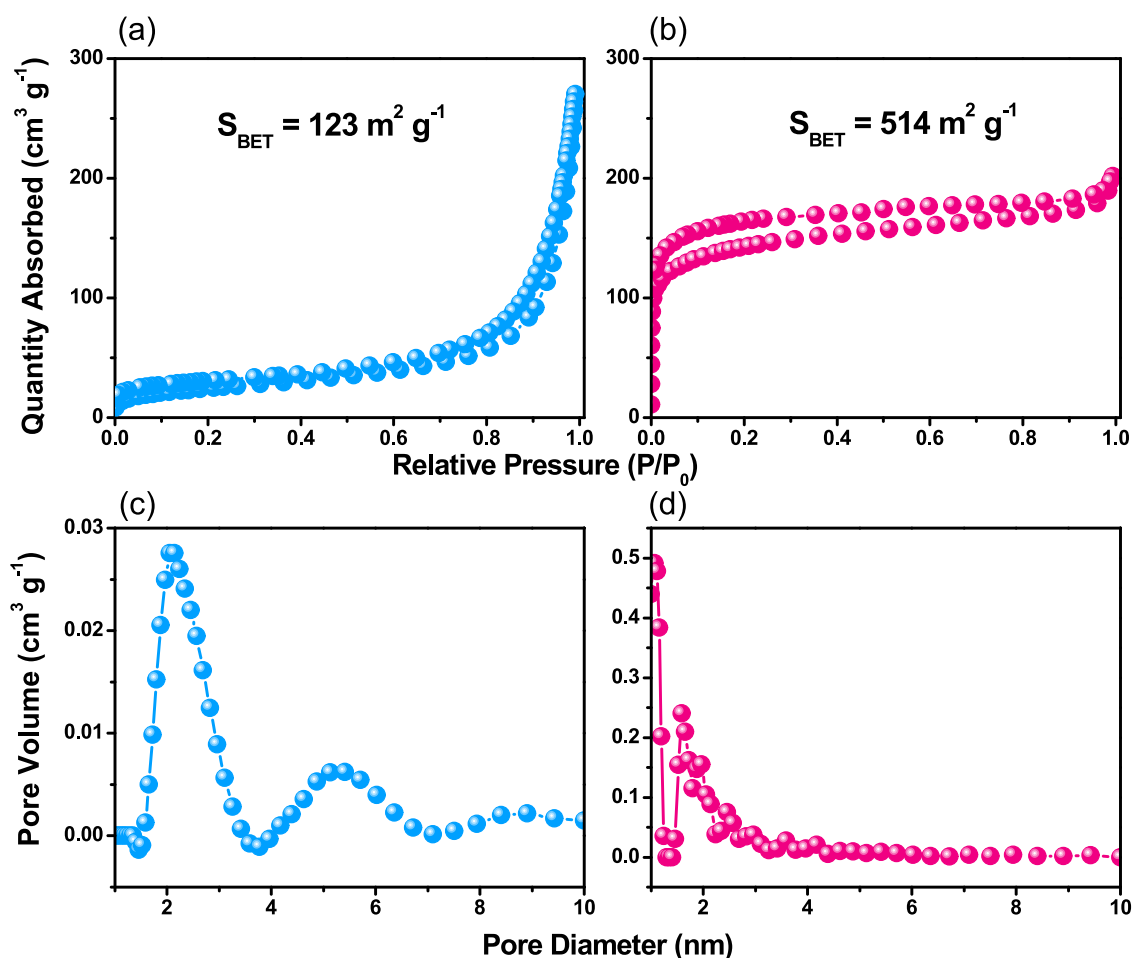
Figure 3. N_2 adsorption/desorption measurements of (a) Py-A-CMP and (b) TPE-A-CMP. Pore size distributions of (c) Py-A-CMP and (d) TPE-A-CMP.

1674, and 1586−1594 cm^{-1} representing the stretching vibrations of aromatic C−H bonds, terminal and internal alkyne groups, and C=O and C=C bonds, respectively. The presence of absorption peaks for C=O groups in the FTIR spectra of both Py-A-CMP and TPE-A-CMP indicated the successful incorporation of redox-active (anthraquinone) moieties in the conjugated frameworks. Furthermore, the signals for the stretching vibrations of the terminal alkyne C−H bonds of Py-T and TPE-T (Figures S9 and S15) were absent in the spectra of both Py-A-CMP and TPE-A-CMP, indicating that complete Sonogashira−Hagihara cross-coupling had occurred between the reactants to form polymeric frameworks. The solid-state ^{13}C NMR spectra confirmed the completeness of the Sonogashira−Hagihara cross-couplings to form the Py-A-CMP and TPE-A-CMP framework structures (Figure 2e,f). The solid-state ^{13}C NMR spectrum of Py-A-CMP featured signals for carbon nuclei at 179.40, 143.65−116.79, and 81.04 ppm, representing the C=O groups in the anthraquinone units, the aromatic −C=C− units, and the alkyne triple bonds, respectively; for TPE-A-CMP, these signals appeared at 180.54, 141.40−120.13, and 80.43 ppm, respectively. Taken together, the FTIR and solid-state ^{13}C NMR spectra confirmed the successful syntheses and introduction of anthraquinone redox units as building blocks in these two CMPs. We used thermogravimetric analysis (TGA) under a N_2 atmosphere to investigate the thermal stability of A-Br$_2$, Py-A-CMP, and TPE-A-CMP in terms of

their thermal degradation temperatures at 10% weight loss (T_{d10}) and residue remaining at 800 °C (char yield). Figure 2g−i reveals that the value of T_{d10} and the char yield of the A-Br$_2$ monomer were 268 °C and 0 wt %, respectively. After polymerization, the value of T_{d10} and the char yield of Py-A-CMP were 435 °C and 58 wt %, respectively; for TPE-A-CMP, they were 539 °C and 53 wt %, respectively. Because of the higher thermal stabilities of both Py-A-CMP and TPE-A-CMP, compared with that of the monomer (A-Br$_2$), after Sonogashira−Hagihara crosslinking, we suspected that these materials would be suitable organic cathode materials for LIBs and that they might have other potential applications in, for example, energy storage. Powder X-ray diffraction (PXRD) patterns (Figure 2j,k) of Py-A-CMP and TPE-A-CMP revealed no crystalline characteristics and no long-range-ordered structures [consistent with the transmission electron microscopy (TEM) images, as seen in the Supporting Information].

We measured the BET specific surface areas (S_{BET}), total pore volumes (V_{total}), and pore size diameters of Py-A-CMP and TPE-A-CMP through N_2 adsorption−desorption analysis at 77 K (Figure 3 and Table S1). The values of S_{BET} and V_{total} for Py-A-CMP were 123 m^2 g^{-1} and 0.41 cm^3 g^{-1}, respectively; for TPE-A-CMP, they were 514 m^2 g^{-1} and 0.31 cm^3 g^{-1}, respectively (Figure 3a,b). In addition, the pore size distribution [determined using nonlocal density functional theory (NL-DFT)] of Py-A-CMP featured dual pore sizes centered at 2.10 and 5.25 nm (Figure 3c), indicating the
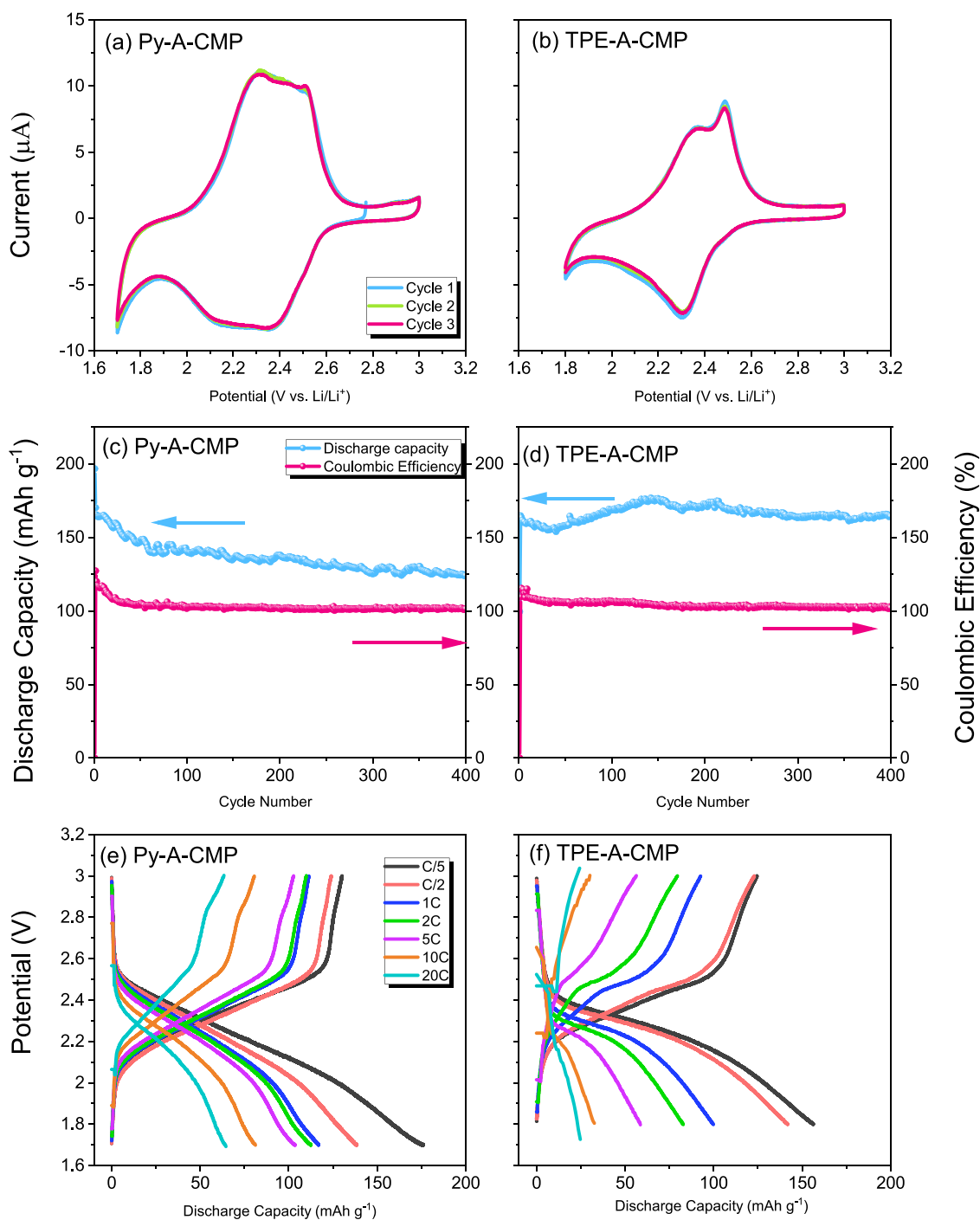
Figure 4. Electrochemical performance of as-prepared cells. CV curves of (a) Py-A-CMP and (b) TPE-A-CMP, recorded at a scan rate of 0.2 mV s^{-1}. Galvanostatic cycle life performance of cells prepared with (c) Py-A-CMP and (d) TPE-A-CMP for 400 cycles at a charge/discharge rate of 0.1C. Galvanostatic discharge profiles of (e) Py-A-CMP and (f) TPE-A-CMP at 0.1C.

presence of a mesoporous architecture. In contrast, the TPE-A-CMP featured a single peak at 1.56 nm (Figure 3d), revealing the presence of a microporous structure. Furthermore, the BET isotherm of Py-A-CMP was a combination of types I and III, according to the IUPAC classification; for TPE-A-CMP, it was a combination of types I and II. The obtained TPE-A-CMP sample had a higher BET surface area than Py-A-CMP, which might be attributed to the molecular orientation of the TPE molecule during the polymerization, which increases the degree of polymerization. Scanning electron microscopy (SEM) images (Figure S27a,b) revealed surface morphologies

of aggregated spherical particles with irregular shapes for Py-A-CMP and aggregated fibers with a highly collapsed network for TPE-A-CMP. Furthermore, the TEM images of both these materials showed they had a uniform microporous structure (Figure S27c,d).

Electrochemical Behavior of Py-A-CMP and TPE-A-CMP as Organic Cathodes for LIBs. Carbonyl compounds are known to possess the ability to store large amounts of energy. Our structural characterization of both the Py-A-CMP and TPE-A-CMP revealed that they possessed abundant quinone groups and high degrees of conjugation, suggesting
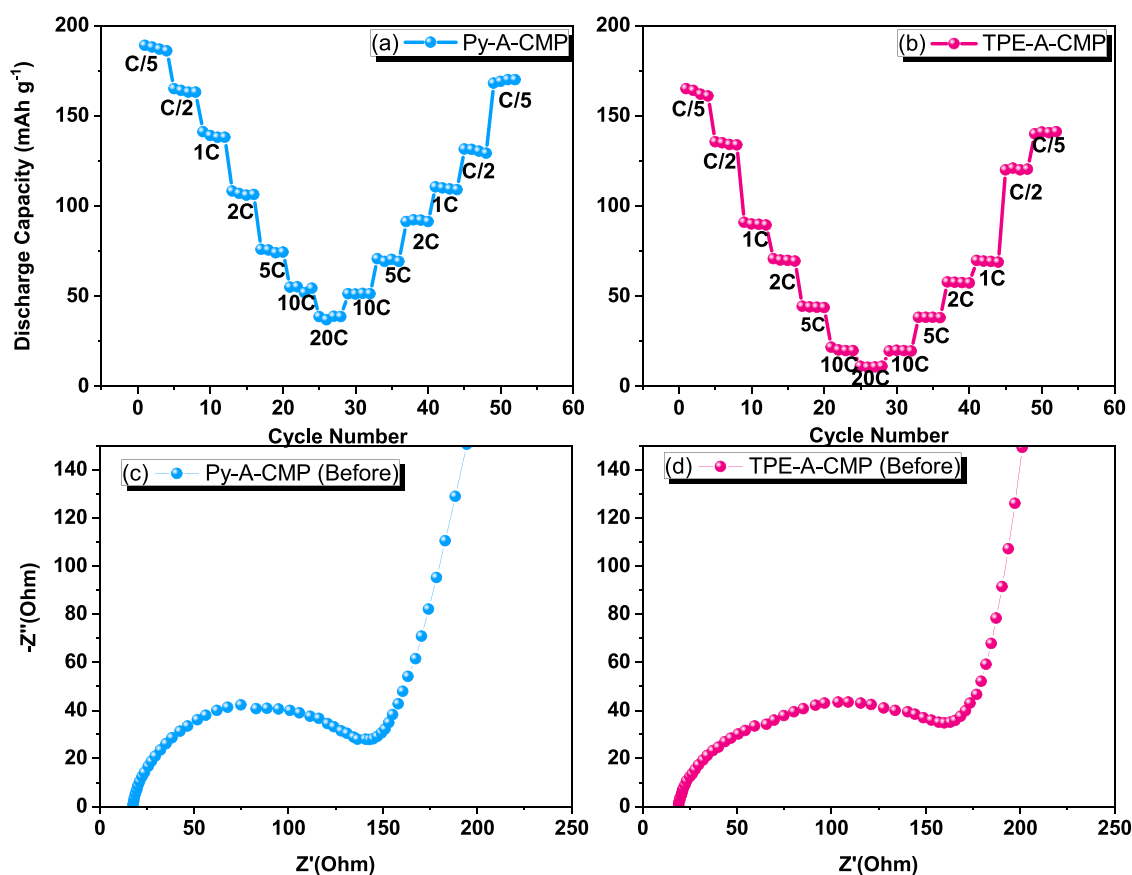
Figure 5. Rate performance of as-prepared cells incorporating (a) Py-A-CMP and (b) TPE-A-CMP, measured at various current densities between 0.2 and 20C. Nyquist plots of cells incorporating (c) Py-A-CMP and (d) TPE-A-CMP, measured before cycling.
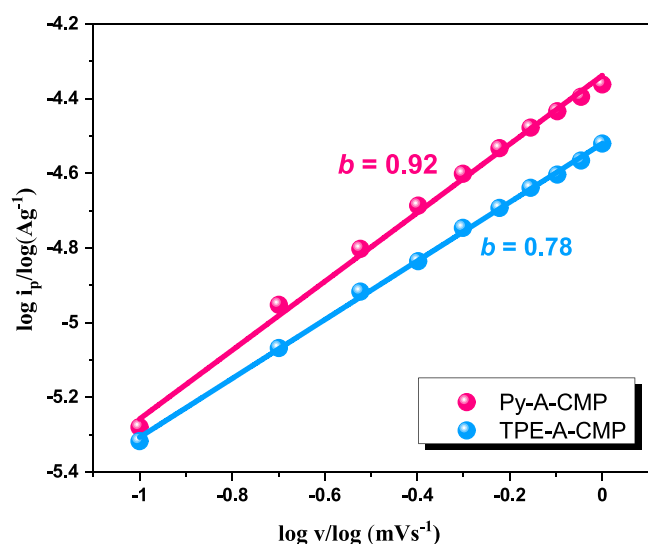

Figure 6. Values of b determined from the relationship between the peak current and the scan rate, plotted as $\log i_p$ with respect to $\log v$.

significant redox activity and the feasibility of preparing high-energy-storage LIBs. We performed various electrochemical measurements of the organic cathodes in the most appropriate electrolyte (1.0 M LiTFSi in DOL/DME) over the potential ranges of 1.7−3.0 V (vs Li/Li⁺) for Py-A-CMP and 1.8−3.0 V (vs Li/Li⁺) for TPE-A-CMP. We evaluated the CV performance of half-cells prepared using Py-A-CMP and TPE-A-CMP as working electrodes and pure Li metal as the counter and

reference electrodes. Figure 4a,b displays the CV profiles of Py-A-CMP and TPE-A-CMP, respectively, measured at a scan rate of 0.2 mV s⁻¹. The profile of Py-A-CMP featured two pairs of weak and strong peaks at 2.51/2.36 and 2.31/2.13 V. The two cathodic peaks near 2.36 and 2.13 V are attributed to the reduction of C=O to C−OLi bonds (lithiation), and the other two anodic peaks at 2.31 and 2.51 V are due to the oxidation of C−OLi to C=O bonds (delithiation). Furthermore, the CV profile of Py-A-CMP exhibited extraordinary overlapping of the CV curves, implying extraordinary electrochemical stability and reversibility of the cell during lithiation and delithiation. The CV profiles of TPE-A-CMP in Figure 4b featured a phenomenon similar to that of Py-A-CMP. The CV curves contained two pairs of strong and weak peaks at 2.49/2.30 and 2.37/2.30 V, respectively. In the cathodic scan, the two peaks at 2.30 V are attributed to the reduction of C=O to C−OLi bonds (lithiation), and the peaks at 2.37 and 2.49 V are due to the oxidation of C−OLi to C=O bonds (delithiation).[59,63] The first three CV cycles exhibit that the curves are almost overlapped, confirming the high electrochemical stability and reversibility of the TPE-A-CMP during the redox reactions. Figure 4c,d displays the galvanostatic cycle life performance of cells at 0.1C with either Py-A-CMP or TPE-A-CMP as an electrode-active material. During the first 50 cycles, both Py-A-CMP and TPE-A-CMP delivered as high discharge capacities as 196.6 and 164.7 mAh g⁻¹, respectively. The comparative increase in the practical discharge capacities to that of the theoretical capacities (181.20 and 162.74 mAh g⁻¹ for Py-A-CMP and TPE-A-CMP, respectively,) of both the electrode materials can be attributed
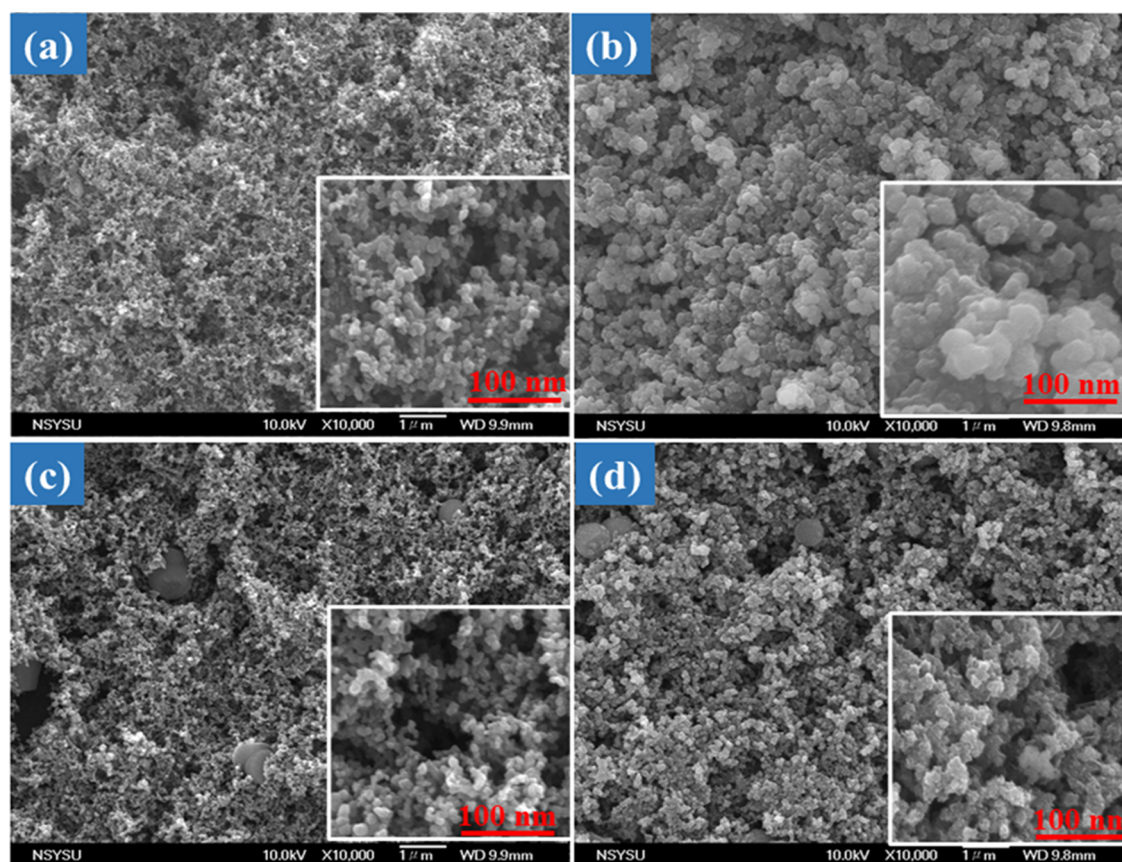
Figure 7. SEM images of prepared cells incorporating Py-A-CMP measured (a) before and (b) after 100 cycles and TPE-A-CMP measured (c) before and (d) after 100 cycles.

to any (or combination) of the following factors: (i) error in weighing of the electrode material, (ii) contribution from the added conductive agents, and (iii) presence of a double layer.[64] During these cycles of the cell incorporating Py-A-CMP, the capacity decreased gradually to 140 mAh g^{-1} from the original capacity; further, as the cycles increased toward 400 cycles, the capacity was maintained at over 120 mAh g^{-1}. In the case of TPE-A-CMP, we observed a gradual increase in the capacity to as high as 178.4 mAh g^{-1}, which can be attributed to the full utilization of available sites for lithiation and delithiation. After 400 charge/discharge cycles, the TPE-A-CMP electrode exhibited a high discharge capacity of 163.6 mAh g^{-1} (99.3% retention) and a high Coulombic efficiency of almost 100%. Figure 4e,f displays the galvanostatic charge/discharge curves of Py-A-CMP and TPE-A-CMP at different C-rates, respectively. Figure 4e features two less-conspicuous discharge/charge plateaus, in good agreement with the CV profiles; similar curves appeared for the cell prepared with TPE-A-CMP, which is in agreement with its CV curves (Figure 4f). The discharge capacities of Py-A-CMP at 0.2, 0.5, 1, 2, 5, 10, and 20C were characterized by discharge capacities of 190.1, 166, 142, 111, 79, 56, and 40 mAh g^{-1}, respectively (Figure 4e). For the TPE-A-CMP, the discharge capacities at 0.2, 0.5, 1, 2, 5, 10, and 20C were 169.2, 138.1, 96.5, 78.4, 49.0, 33.6, and 19.0 mAh g^{-1}, respectively (Figure 4f). Both cells exhibited considerable rate performances with high discharge capacities.

Furthermore, Figure 5a shows a reversible high capacity of 160 mAh g^{-1} when the current density returned to 0.2C after long-term cycling. Figure 5b shows that the discharge capacity

quickly returned to 168 mAh g^{-1} when the specific current returned to 0.2C after cycling. In both cases, when the current density returned to 0.2C, the discharge capacities were closer to their initial capacities. Moreover, both compounds exhibited good rate capability performance, but the discharge capacities of Py-A-CMP were higher than those of the TPE-A-CMP. Next, we used electrochemical impedance spectroscopy (EIS) to investigate both samples before cycling (Figure 5c,d for Py-A-CMP and TPE-A-CMP, respectively). The spectra suggested that the resistance of Py-A-CMP is lower than that of TPE-A-CMP.

The charge-transfer resistances (R_{ct}) of Py-A-CMP and TPE-A-CMP are 154 and 170 Ω, respectively, which explains why the Py-A-CMP electrode exhibits better C-rate performance. Interestingly, the electrochemical performance of these compounds was good when compared with that of similar types of compounds reported previously as cathode materials for high-energy-storage LIBs. The AC impedance characteristics suggested that our compounds would be ideal candidates for use in high-performance LIBs due to their highly porous network structures, which would facilitate the conduction of Li ions. Therefore, we extended our study to investigate the reaction kinetics of the Py-A-CMP- and TPE-A-CMP-based cathode materials for LIBs, by recording their CV curves at various sweep rates between 0.1 and 1.0 mV s^{-1}, as shown in Figure S28a,b for CV curves at different scan rates. The evolution of the CV curves upon increasing the sweep rate corresponded to a linear increase in the current, governed by the following equations.[65]
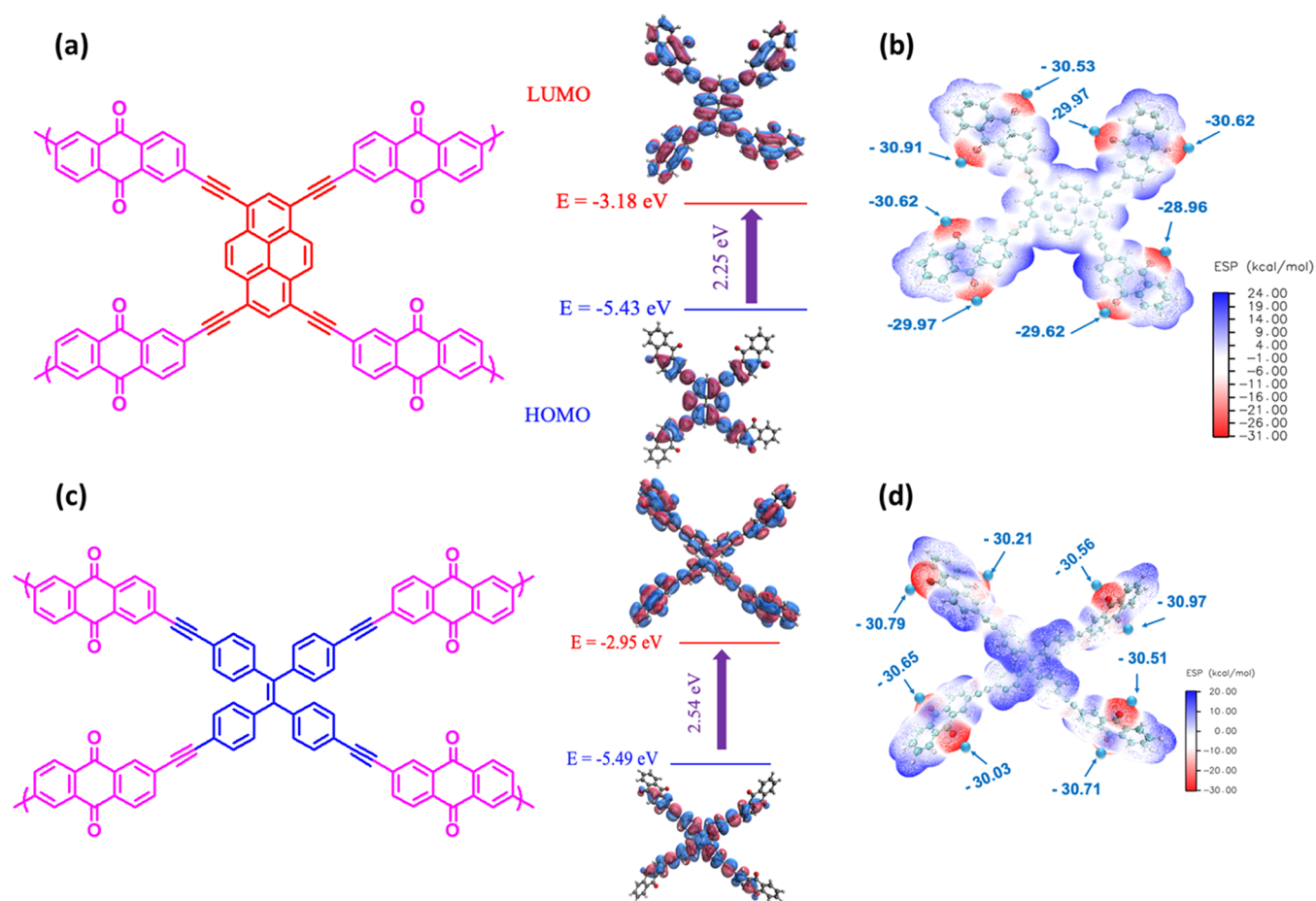
Figure 8. Highest occupied molecular orbital (HOMO) and LUMO distributions of (a) Py-A-CMP and (b) TPE-A-CMP, along with their energies and band gaps, determined at the B3LYP/6-31G(d) level of theory. Molecular electrostatic potentials (MESPs) of (c) Py-A-CMP and (d) TPE-A-CMP, measured at the B3LYP/6-31G(d) level of theory.

$$i = av^b \tag{1}$$

$$\log i = \log a + b \log v \tag{2}$$

where i is the peak current, v is the scan rate, and a and b are arbitrary constants. The fitted curve of $\log v$ with respect to $\log i$ describes the value of constant b, which demonstrates whether the cell is diffusive or capacitive in nature. If the value of b approaches 1, it implies capacitive behavior; if it is close to 0.5, it represents the diffusive behavior of cells incorporating CMP-based polymers. Figure 6 reveals that the calculated values of b for Py-A-CMP and TPE-A-CMP were 0.92 and 0.79, respectively. Because both values were greater than 0.5, a significant portion of the capacitive behavior dominated the total capacity of the cell because of the presence of redox-active moieties in both compounds. Thus, most of the capacity originated from the capacitive behavior, implying fast kinetics of Li⁺ ions in the energy storage devices.[59]

Furthermore, to investigate the structural stability of the prepared Py-A-CMP and TPE-A-CMP electrodes, we recorded their SEM images before and after 100 deep charge/discharge cycles (Figure 7). Both cathode materials maintained their pristine morphologies, which were also confirmed with the formation of solid electrolyte interphases (SEIs) on the electrode surfaces. Moreover, no significant variations in thickness or any signs of crack-growth initiation were evident from the cross sections of each electrode, even after 100 cycles, confirming the compact structures of both the Py-A-CMP and

TPE-A-CMP electrodes. We attribute the extraordinary long-term cycling capability of both electrodes to the excellent stability of their CMP-based polymer networks by virtue of their highly porous network structures providing large free spaces for Li⁺ ions during lithiation and delithiation, thereby not only improving the cycling stability but also preventing the dissolution of the electrode materials in the electrolyte solution.

We used density functional theory (DFT) to examine the electronic structure of the polymers and provide further insight into the improved electrochemical performance of the two polymers. The electronic structure is an essential factor in the charge storage ability and redox properties of CMPs. The hybrid functional B3LYP was used with the basis set 6-31G(d). The dispersion correction D3BJ was used, which is necessary to account for long-range and noncovalent interactions. We considered several conformers for the ground-state geometry of the monomers and selected the one with the lowest energy. We then used the harmonic vibrational frequency to confirm this global minimum. Calculations of the highest occupied molecular orbital−lowest unoccupied molecular orbital (HOMO−LUMO) energy gap and molecular electrostatic potential (MESP) were done on the optimized geometries at the same level of theory. Figure 8a,b displays the frontier molecular orbitals of Py-A-CMP and TPE-A-CMP. For both polymers, the lowest unoccupied molecular orbital (LUMO) was highly delocalized and spread over the whole molecule.

The distribution of the LUMO has an essential impact on the electrochemical performance of any polymer; moreover, a small band gap for a polymer implied higher electron conductivity. Figure 8c,d presents the molecular electrostatic potential (MESP) analyses of the two polymers. High delocalization led to decreasing charge density over the redox-active sites (C=O groups in both polymers). Low negative-charge density around the active sites could weaken their interactions with Li$^+$ ions, leading to faster diffusion of Li$^+$ ions through the CMP pores. Both polymers featured extended π-conjugation (leading to better electron conduction), highly delocalized LUMO distributions, small band gaps, and decreased negative-charge density at their active sites (C=O groups). These factors resulted in these polymers displaying improved electrochemical performance, higher electron mobilities, and better diffusion of Li$^+$ ions, ensuring higher charge storage abilities with enhanced cycling and rate performance and low degrees of self-discharge over time. Thus, these C=O group-enriched polymers functioned as reliable cathode materials for high-performance LIBs. As presented in Table S2, our two new materials Py-A-CMP and TPE-A-CMP displayed excellent performance when employed as cathode materials in LIBs, when compared with other reported C=O group-based materials, including DAAQ-COF (145 mAh g^{-1}),[66] IEP11-E12 (21.3 mAh g^{-1}),[48] Tb-DANT-COF (80.1 mAh g^{-1}),[67] BQbTPL (95.8 mAh g^{-1}),[63] DTP-ANDI-COF (21 mAh g^{-1}),[68] AQ (100 mAh g^{-1}),[69] HATN-CMP (147 mAh g^{-1}),[60] PT-BTA (166.7 mAh g^{-1}),[59] and P15AQ (148 mAh g^{-1}).[70]

CONCLUSIONS

We have used Sonogashira−Hagihara coupling to construct two types of CMPs featuring anthraquinone moieties as their redox-active groups. We investigated the chemical structures, porosities, thermal stabilities, theoretical characteristics, and morphologies of these two CMPs. When we applied Py-T-CMP and TPE-T-CMP as organic cathode materials, the LIBs exhibited outstanding high discharge capacities of 196.6 and 164.7 mAh g^{-1} at 0.1C, respectively, with good rate capability performance arising from the presence of active C=O groups, poor solubility, and highly conjugation structures. Both of these CMP materials have the ability to deliver high performance for energy storage devices, and they have the potential to become important materials when used as CMPs that afford 3D polymeric network structures facilitating redox mechanisms. Finally, our new CMP materials appear to be better organic cathode materials for LIBs, when compared with other previously reported porous CMPs.

ASSOCIATED CONTENT

Ⓢ Supporting Information

The Supporting Information is available free of charge at https://pubs.acs.org/doi/10.1021/acsaem.1c03270.

> Details of the synthesis method of 1,3,6,8-tetrabromo-pyrene (Py-Br$_4$), tetraphenylethylene (TPE), and 1,1,2,2-tetrakis(4-bromophenyl)ethene (TPE-Br$_4$) and schematic synthesis of Py-T, TPE-T, and A-Br$_2$; FTIR and NMR figures of the synthesized monomers; CV curves at different scan rates as well as different rate capability profiles of both electrode materials; BET and TGA analyses of A-Br$_2$, Py-A-CMP, and TPE-A-CMP (Table S1); comparison between Py-A-CMP, TPE-A-

CMP, and other reported carbonyl-based materials for LIBs (Table S2) (PDF)

■ AUTHOR INFORMATION

Corresponding Authors

Mohamed Gamal Mohamed − *Department of Materials and Optoelectronic Science, Center for Functional Polymers and Supramolecular Materials and Center of Crystal Research, National Sun Yat-Sen University, Kaohsiung 80424, Taiwan; Chemistry Department, Faculty of Science, Assiut University, Assiut 71516, Egypt;* orcid.org/0000-0003-0301-8372; Email: mgamal.eldin34@gmail.com

Jyh-Tsung Lee − *Department of Chemistry, National Sun Yat-Sen University, Kaohsiung 80424, Taiwan;* Email: jtlee@faculty.nsysu.edu.tw

Shiao Wei-Kuo − *Department of Materials and Optoelectronic Science, Center for Functional Polymers and Supramolecular Materials and Center of Crystal Research, National Sun Yat-Sen University, Kaohsiung 80424, Taiwan; Department of Medicinal and Applied Chemistry, Kaohsiung Medical University, Kaohsiung 807, Taiwan;* orcid.org/0000-0002-4306-7171; Email: kuosw@faculty.nsysu.edu.tw

Authors

Santosh U. Sharma − *Department of Chemistry, National Sun Yat-Sen University, Kaohsiung 80424, Taiwan*

Cheng-Han Yang − *Department of Materials and Optoelectronic Science, Center for Functional Polymers and Supramolecular Materials and Center of Crystal Research, National Sun Yat-Sen University, Kaohsiung 80424, Taiwan*

Maha Mohamed Samy − *Department of Materials and Optoelectronic Science, Center for Functional Polymers and Supramolecular Materials and Center of Crystal Research, National Sun Yat-Sen University, Kaohsiung 80424, Taiwan; Chemistry Department, Faculty of Science, Assiut University, Assiut 71516, Egypt*

Ahmed A. K. Mohammed − *Chemistry Department, Faculty of Science, Assiut University, Assiut 71516, Egypt*

Swetha V. Chaganti − *Department of Chemistry, National Sun Yat-Sen University, Kaohsiung 80424, Taiwan*

Complete contact information is available at:
https://pubs.acs.org/10.1021/acsaem.1c03270

Author Contributions

[⊥]M.G.M. and S.U.S. contributed equally to this work.

Notes

The authors declare no competing financial interest.

■ ACKNOWLEDGMENTS

■ REFERENCES

(1) Kim, J.; Kim, J. H.; Ariga, K. Redox-Active Polymers for Energy Storage Nanoarchitectonics. *Joule* 2017, *1*, 739−768.

(2) Xue, X.; Luo, J.; Kong, L.; Zhao, J.; Zhang, Y.; Du, H.; Chen, S.; Xie, Y. The synthesis of triazine−thiophene−thiophene conjugated

porous polymers and their composites with carbon as anode materials in lithium-ion batteries. *RSC Adv.* **2021**, *11*, 10688−10698.

(3) Zhang, C.; He, Y.; Mu, P.; Wang, X.; He, Q.; Chen, Y.; Zeng, J.; Wang, F.; Xu, Y.; Xing, J. Toward High Performance Thiophene-Containing Conjugated Microporous Polymer Anodes for Lithium-Ion Batteries through Structure Design. *Adv. Funct. Mater.* **2018**, *28*, No. 1705432.

(4) Zhang, S.; Huang, W.; Hu, P.; Huang, C.; Shang, C.; Zhang, C.; Yang, R.; Cui, G. Conjugated microporous polymers with excellent electrochemical performance for lithium and sodium storage. *J. Mater. Chem. A* **2015**, *3*, 1896−1901.

(5) Li, M.; Lu, J.; Chen, Z.; Amine, K. 30 Years of Lithium-Ion Batteries. *Adv. Mater.* **2018**, *30*, No. 1800561.

(6) Liu, W.; Song, M. S.; Kong, B.; Cui, Y. Flexible and Stretchable Energy Storage: Recent Advances and Future Perspectives. *Adv. Mater.* **2017**, *29*, No. 1603436.

(7) Schmuch, R.; Wagner, R.; Hörpel, G.; Placke, T.; Winter, M. Performance and cost of materials for lithium-based rechargeable automotive batteries. *Nat. Energy* **2018**, *3*, 267−278.

(8) De, A.; Das, S.; Samanta, A. Hot Hole Transfer Dynamics from CsPbBr3 Perovskite Nanocrystals. *ACS Energy Lett.* **2020**, *5*, 2246−2252.

(9) Larcher, D.; Tarascon, J. M. Towards greener and more sustainable batteries for electrical energy storage. *Nat. Chem.* **2015**, *7*, 19−29.

(10) Liu, Y. C.; Yeh, L. H.; Zheng, M. J.; Wu, K. C. W. Highly selective and high-performance osmotic power generators in subnanochannel membranes enabled by metal-organic frameworks. *Sci. Adv.* **2021**, *7*, No. eabe9924.

(11) Wang, J.; Chen, C. S.; Zhang, Y. Hexaazatrinaphthylene-Based Porous Organic as Organic Cathode Materials for Polymers Lithium-Ion Batteries. *ACS Sustainable Chem. Eng.* **2018**, *6*, 1772−1779.

(12) Armand, M.; Grugeon, S.; Vezin, H.; Laruelle, S.; Ribière, P.; Poizot, P.; Tarascon, J. M. Conjugated dicarboxylate anodes for Li-ion batteries. *Nat. Mater.* **2009**, *8*, 120−125.

(13) Wang, H. G.; Li, Q.; Wu, Q.; Si, Z.; Lv, X.; Liang, X.; Wang, H.; Sun, L.; Shi, W.; Song, S. Conjugated Microporous Polymers with Bipolar and Double Redox-Active Centers for High-Performance Dual-Ion, Organic Symmetric Battery. *Adv. Energy Mater.* **2021**, *11*, No. 2100381.

(14) Shi, Y.; Zhou, X.; Zhang, J.; Bruck, A. M.; Bond, A. C.; Marschilok, A. C.; Takeuchi, K. J.; Takeuchi, E. S.; Yu, G. Nanostructured Conductive Polymer Gels as a General Framework Material To Improve Electrochemical Performance of Cathode Materials in Li-Ion Batteries. *Nano Lett.* **2017**, *17*, 1906−1914.

(15) Xu, N.; Mei, S.; Chen, Z.; Dong, Y.; Li, W.; Zhang, C. High-performance Li-organic battery based on thiophene-containing porous organic polymers with different morphology and surface area as the anode materials. *Chem. Eng. J* **2020**, *395*, No. 124975.

(16) Hong, J.; Lee, M.; Lee, B.; Seo, D. H.; Park, C. B.; Kang, K. Biologically inspired pteridine redox centres for rechargeable batteries. *Nat. Commun.* **2014**, *5*, No. 5335.

(17) Schon, T. B.; Tilley, A. J.; Bridges, C. R.; Miltenburg, M. B.; Seferos, D. S. Bio-Derived Polymers for Sustainable Lithium-Ion Batteries. *Adv. Funct. Mater.* **2016**, *26*, 6896−6903.

(18) Peng, C.; Ning, G. H.; Su, J.; Zhong, G.; Tang, W.; Tian, B.; Su, C.; Yu, D.; Zu, L.; Yang, J. M.; Ng, F.; Hu, Y. S.; Yang, Y.; Armand, M.; Loh, K. P. Reversible multi-electron redox chemistry of π-conjugated N-containing heteroaromatic molecule-based organic cathodes. *Nat. Energy* **2017**, *2*, No. 17074.

(19) Jaffe, A.; Valdes, A. S.; Karunadasa, H. I. Quinone-Functionalized Carbon Black Cathodes for Lithium Batteries with High Power Densities. *Chem. Mater.* **2015**, *27*, 3568−3571.

(20) Oyaizu, K.; Choi, W.; Nishide, H. Functionalization of poly(4-chloromethylstyrene) with anthraquinone pendants for organic anode-active materials. *Polym. Adv. Technol.* **2011**, *22*, 1242−1247.

(21) Samy, M. M.; Mohamed, M. G.; Mansoure, T. T.; Meng, T. S.; Khan, M. A. R.; Liaw, C. C.; Kuo, S. W. Solid State Chemical Transformations through Ring-Opening Polymerization of Ferrocene-Based Conjugated Microporous Polymers in Host−Guest Complexes with Benzoxazine-Linked Cyclodextrin. *J. Taiwan Inst. Chem. Eng.* **2021**, DOI: 10.1016/j.jtice.2021.10.010.

(22) Mulzer, C. R.; Shen, L.; Bisbey, R. P.; McKone, J. R.; Zhang, N.; Abruña, H. D.; Dichtel, W. R. Superior Charge Storage and Power Density of a Conducting Polymer-Modified Covalent Organic Framework. *ACS Cent. Sci.* **2016**, *2*, 667−673.

(23) Wang, Y.; Song, Y.; Xia, Y. Electrochemical capacitors: mechanism, materials, systems, characterization and applications. *Chem. Soc. Rev.* **2016**, *45*, 5925−5950.

(24) Mohamed, M. G.; Ahmed, M. M. M.; Du, W. T.; Kuo, S. W. Meso/Microporous Carbons from Conjugated Hyper-Crosslinked Polymers Based on Tetraphenylethene for High-Performance CO2 Capture and Supercapacitor. *Molecules* **2021**, *26*, No. 738.

(25) Elewa, A. M.; EL-Mahdy, A. F. M.; Elsayed, M. H.; Mohamed, M. G.; Kuo, S. W.; Chou, H. H. Sulfur-doped triazine-conjugated microporous polymers for achieving the robust visible-light-driven hydrogen evolution. *Chem. Eng. J.* **2021**, *421*, No. 129825.

(26) Mohamed, M. G.; Tsai, M. Y.; Wang, C. F.; Huang, C. F.; Danko, M.; Dai, L.; Chen, T.; Kuo, S. W. Multifunctional Polyhedral Oligomeric Silsesquioxane (POSS) Based Hybrid Porous Materials for CO2 Uptake and Iodine Adsorption. *Polymers* **2021**, *13*, No. 221.

(27) Samy, M. M.; Mohamed, M. G.; Kuo, S. W. Directly synthesized nitrogen-and-oxygen−doped microporous carbons derived from a bio-derived polybenzoxazine exhibiting high-performance supercapacitance and CO2 uptake. *Eur. Polym. J.* **2020**, *138*, No. 109954.

(28) Mohamed, M. G.; Atayde, E. C., Jr.; Matsagar, B. M.; Na, J.; Yamauchi, Y.; Wu, K. C. W.; Kuo, S. W. Construction Hierarchically Mesoporous/Microporous Materials Based on Block Copolymer and Covalent Organic Framework. *J. Taiwan Inst. Chem. Eng.* **2020**, *112*, 180−192.

(29) Shin, E. S.; Go, J. Y.; Ryu, G. S.; Liu, A.; Noh, Y. Y. Highly Reliable Organic Field-Effect Transistors with Molecular Additives for a High-Performance Printed Gas Sensor. *ACS Appl. Mater. Interfaces* **2021**, *13*, 4278−4283.

(30) Mohamed, M. G.; Chen, T. C.; Kuo, S. W. Solid-State Chemical Transformations to Enhance Gas Capture in Benzoxazine-Linked Conjugated Microporous Polymers. *Macromolecules* **2021**, *54*, 5866−5877.

(31) Samy, M. M.; Mohamed, M. G.; Kuo, S. W. Pyrene-functionalized tetraphenylethylene polybenzoxazine for dispersing single-walled carbon nanotubes and energy storage. *Compos. Sci. Technol.* **2020**, *199*, No. 108360.

(32) Mohamed, M. G.; Elsayed, M. H.; Elewa, A. M.; EL-Mahdy, A. F. M.; Yang, C. H.; Mohammed, A. A. K.; Chou, H. H.; Kuo, S. W. Pyrene-containing conjugated organic microporous polymers for photocatalytic hydrogen evolution from water. *Catal. Sci. Technol.* **2021**, *11*, 2229−2241.

(33) Mohamed, M. G.; Liu, N. Y.; EL-Mahdy, A. F. M.; Kuo, S. W. Ultrastable luminescent hybrid microporous polymers based on polyhedral oligomeric silsesquioxane for CO2 uptake and metal ion sensing. *Microporous Mesoporous Mater.* **2021**, *311*, No. 110695.

(34) Aly, K. I.; Sayed, M. M.; Mohamed, M. G.; Kuo, S. W.; Younis, O. A facile synthetic route and dual function of network luminescent porous polyester and copolyester containing porphyrin moiety for metal ions sensor and dyes adsorption. *Microporous Mesoporous Mater.* **2020**, *298*, No. 110063.

(35) Samy, M. M.; Mohamed, M. G.; El-Mahdy, A. F. M.; Mansoure, T. H.; Wu, K. C. W.; Kuo, S. W. High-Performance Supercapacitor Electrodes Prepared From Dispersions of Tetrabenzonaphthalene-Based Conjugated Microporous Polymers and Carbon Nanotubes. *ACS Appl. Mater. Interfaces* **2021**, *13*, 51906−51916.

(36) Mohamed, M. G.; Lee, C. C.; EL-Mahdy, A. F. M.; Lüder, J.; Yu, M. H.; Li, Z.; Zhu, Z.; Chueh, C. C.; Kuo, S. W. Exploitation of two-dimensional conjugated covalent organic frameworks based on tetraphenylethylene with bicarbazole and pyrene units and applications in perovskite solar cells. *J. Mater. Chem. A* **2020**, *8*, 11448−11459.

(37) EL-Mahdy, A. F. M.; Elewa, A. M.; Huang, S. W.; Chou, H. H.; Kuo, S. W. Dual-Function Fluorescent Covalent Organic Frameworks: HCl Sensing and Photocatalytic H2 Evolution from Water. *Adv. Opt. Mater.* **2020**, *8*, No. 2000641.

(38) EL-Mahdy, A. F. M.; Young, C.; Kim, J.; You, J.; Yamauchi, Y.; Kuo, S. W. Hollow Microspherical and Microtubular [3+ 3] Carbazole-Based Covalent Organic Frameworks and Their Gas and Energy Storage Applications. *ACS Appl. Mater. Interfaces* **2019**, *11*, 9343–9354.

(39) Mohamed, M. G.; EL-Mahdy, A. F. M.; Kotp, M. G.; Kuo, S. W. Advances in Porous Organic Polymers: Syntheses, Structures, and Diverse Applications. *Mater. Adv.* **2022**, DOI: 10.1039/D1MA00771H.

(40) Casado, N.; Hernández, G.; Sardon, H.; Mecerreyes, D. Current trends in redox polymers for energy and medicine. *Prog. Polym. Sci.* **2016**, *52*, 107–135.

(41) Inoue, S.; Minemawari, H.; Tsutsumi, J.; Chikamatsu, M.; Yamada, T.; Horiuchi, S.; Tanaka, M.; Kumai, R.; Yoneya, M.; Hasegawa, T. Effects of Substituted Alkyl Chain Length on Solution-Processable Layered Organic Semiconductor Crystals. *Chem. Mater.* **2015**, *27*, 3809–3812.

(42) Salunkhe, R. R.; Tang, J.; Kobayashi, N.; Kim, J.; Ide, Y.; Tominaka, S.; Kim, J. H.; Yamauchi, Y. Ultrahigh performance supercapacitors utilizing core–shell nanoarchitectures from a metal–organic framework-derived nanoporous carbon and a conducting polymer. *Chem. Sci.* **2016**, *7*, 5704–5713.

(43) Shi, Y.; Yu, G. Designing Hierarchically Nanostructured Conductive Polymer Gels for Electrochemical Energy Storage and Conversion. *Chem. Mater.* **2016**, *28*, 2466–2477.

(44) Häupler, B.; Wild, A.; Schubert, U. S. Carbonyls: Powerful Organic Materials for Secondary Batteries. *Adv. Energy Mater.* **2015**, *5*, No. 1402034.

(45) Kim, K. C.; Liu, T.; Lee, S. W.; Jang, S. S. First-Principles Density Functional Theory Modeling of Li Binding: Thermodynamics and Redox Properties of Quinone Derivatives for Lithium-Ion Batteries. *J. Am. Chem. Soc.* **2016**, *138*, 2374–2382.

(46) Liang, Y.; Tao, Z.; Chen, J. Organic Electrode Materials for Rechargeable Lithium Batteries. *Adv. Energy Mater.* **2012**, *2*, 742–769.

(47) Mohamed, M. G.; Mnanoure, T. H.; Takashi, Y.; Samy, M. M.; Chen, T.; Kuo, S. W. Ultrastable Porous Organic/Inorganic Polymers Based on Polyhedral Oligomeric Silsesquioxane (POSS) Hybrids Exhibiting High Performance for Thermal Property and Energy Storage. *Microporous Mesoporous Mater.* **2021**, *328*, No. 111505.

(48) Molina, A.; Patil, N.; Ventosa, E.; Liras, M.; Palma, J.; Marcilla, R. New Anthraquinone-Based Conjugated Microporous Polymer Cathode with Ultrahigh Specific Surface Area for High-Performance Lithium-Ion Batteries. *Adv. Funct. Mater.* **2020**, *30*, No. 1908074.

(49) Rasheev, H. G.; Araujo, R. B.; Tadjer, A.; Johansson, P. Fundamental promise of anthraquinone functionalized graphene based next generation battery electrodes: a DFT study. *J. Mater. Chem. A* **2020**, *8*, 14152–14161.

(50) Son, E. J.; Kim, J. H.; Kima, K.; Park, C. B. Quinone and its derivatives for energy harvesting and storage materials. *J. Mater. Chem. A* **2016**, *4*, 11179–11202.

(51) Sotomura, T.; Uemachi, H.; Takeyama, K.; Naoi, K.; Oyama, N. New organodisulfide—polyaniline composite cathode for secondary lithium battery. *Electrochim. Acta* **1992**, *37*, 1851–1854.

(52) Wu, Y.; Zeng, R.; Nan, J.; Shu, D.; Qiu, Y.; Chou, S. L. Quinone Electrode Materials for Rechargeable Lithium/Sodium Ion Batteries. *Adv. Energy Mater.* **2017**, *7*, No. 1700278.

(53) Zhao, Q.; Zhu, Z.; Chen, J. Molecular Engineering with Organic Carbonyl Electrode Materials for Advanced Stationary and Redox Flow Rechargeable Batteries. *Adv. Mater.* **2017**, *29*, No. 1607007.

(54) Chen, L.; Yang, Y.; Jiang, D. CMPs as Scaffolds for Constructing Porous Catalytic Frameworks: A Built-in Heterogeneous Catalyst with High Activity and Selectivity Based on Nanoporous Metalloporphyrin Polymers. *J. Am. Chem. Soc.* **2010**, *132*, 9138–9143.

(55) Abuzeid, H. R.; EL-Mahdy, A. F. M.; Kuo, S. W. Covalent organic frameworks: Design principles, synthetic strategies, and diverse applications. *Giant* **2021**, *6*, No. 100054.

(56) Liu, X.; Xu, Y.; Jiang, D. Conjugated Microporous Polymers as Molecular Sensing Devices: Microporous Architecture Enables Rapid Response and Enhances Sensitivity in Fluorescence-On and Fluorescence-Off Sensing. *J. Am. Chem. Soc.* **2012**, *134*, 8738–8741.

(57) Liras, M.; Iglesias, M.; Sánchez, F. Conjugated Microporous Polymers Incorporating BODIPY Moieties as Light-Emitting Materials and Recyclable Visible-Light Photocatalysts. *Macromolecules* **2016**, *49*, 1666–1673.

(58) Zhang, B.; Wang, W.; Liang, L.; Xu, Z.; Li, X.; Qiao, S. Prevailing conjugated porous polymers for electrochemical energy storage and conversion: Lithium-ion batteries, supercapacitors and water-splitting. *Coord. Chem. Rev.* **2021**, *436*, No. 213782.

(59) Li, K.; Li, Q.; Wang, Y.; Wang, H. G.; Li, Y.; Si, Z. An aromatic carbonyl compound-linked conjugated microporous polymer as an advanced cathode material for lithium-organic batteries. *Mater. Chem. Front.* **2020**, *4*, 2697–2703.

(60) Xu, F.; Chen, X.; Tang, Z.; Wu, D.; Fu, R.; Jiang, D. Redox-active conjugated microporous polymers: a new organic platform for highly efficient energy storage. *Chem. Commun.* **2014**, *50*, 4788–4790.

(61) Zhao, L.; Yu, J.; Xing, C.; Ullah, Z.; Yu, C.; Zhu, S.; Chen, M.; Li, W.; Li, Q.; Liu, L. Nanopore confined anthraquinone in MOF-derived N-doped microporous carbon as stable organic cathode for lithium-ion battery. *Energy Storage Mater.* **2019**, *22*, 433–440.

(62) Wu, C.; Hu, M.; Yan, X.; Shan, G.; Liu, J.; Yang, J. Azo-linked covalent triazine-based framework as organic cathodes for ultrastable capacitor-type lithium-ion batteries. *Energy Storage Mater.* **2021**, *36*, 347–354.

(63) Ouyang, Z.; Tranca, D.; Zhao, Y.; Chen, Z.; Fu, X.; Zhu, J.; Zhai, G.; Ke, C.; Kymakis, E.; Zhuang, X. Quinone-Enriched Conjugated Microporous Polymer as an Organic Cathode for Li-Ion Batteries. *ACS Appl. Mater. Interfaces* **2021**, *13*, 9064–9073.

(64) Häupler, B.; Hagemann, T.; Friebe, C.; Wild, A.; Schuber, U. S. Dithiophenedione-Containing Polymers for Battery Application. *ACS Appl. Mater. Interfaces* **2015**, *7*, 3473–3479.

(65) Guo, K.; Xi, B.; Wei, R.; Li, H.; Feng, J.; Xiong, S. Hierarchical Microcables Constructed by CoP@C⊂Carbon Framework Intertwined with Carbon Nanotubes for Efficient Lithium Storage. *Adv. Energy Mater.* **2020**, *10*, No. 1902913.

(66) Wang, S.; Wang, Q.; Shao, P.; Han, Y.; Gao, X.; Ma, L.; Yuan, S.; Ma, X.; Zhou, J.; Feng, X.; Wang, B. Exfoliation of Covalent Organic Frameworks into Few-Layer Redox-Active Nanosheets as Cathode Materials for Lithium-Ion Batteries. *J. Am. Chem. Soc.* **2017**, *139*, 4258–4261.

(67) Yang, D. H.; Yao, Z. Q.; Wu, D.; Zhang, Y. H.; Zhou, Z.; Bu, X. H. Structure- Modulated Crystalline Covalent Organic Frameworks as High-Rate Cathodes for Li- Ion Batteries. *J. Mater. Chem. A* **2016**, *4*, 18621–18627.

(68) Xu, F.; Jin, S.; Zhong, H.; Wu, D.; Yang, X.; Chen, X.; Wei, H.; Fu, R.; Jiang, D. Electrochemically Active, Crystalline, Mesoporous Covalent Organic Frameworks on Carbon Nanotubes for Synergistic Lithium-Ion Battery Energy Storage. *Sci. Rep.* **2015**, *5*, No. 8225.

(69) Song, Z.; Zhan, H.; Zhou, Y. Anthraquinone Based Polymer as High Performance Cathode Material for Rechargeable Lithium Batteries. *Chem. Commun.* **2009**, *104*, 448–450.

(70) Song, Z.; Qian, Y.; Gordin, M. L.; Tang, D.; Xu, T.; Otani, M.; Zhan, H.; Zhou, H.; Wang, D. Polyanthraquinone as a Reliable Organic Electrode for Stable and Fast Lithium Storage. *Angew. Chem., Int. Ed.* **2015**, *54*, 13947–13951.